The influence of secondary solvents on the morphology of spiro-MeOTAD hole transport layer for lead halide perovskite solar cells.

Luis K. Ono[†], Zafer Hawash[†], Emilio J. Juarez-Perez[†], Longbin Qiu[†], Yan Jiang[†], and Yabing Qi[†,*]

[†] Energy Materials and Surface Sciences Unit (EMSSU), Okinawa Institute of Science and Technology Graduate University (OIST), 1919-1 Tancha, Onna-son, Kunigami-gun, Okinawa 904-0495, Japan

Abstract

2,2',7,7'-Tetrakis(N,N-di-p-methoxyphenylamine)-9,9'-spirobifluorene (spiro-MeOTAD) has been widely employed as hole transport layer (HTL) in perovskite-based solar cells. Despite high efficiencies, issues have been reported regarding solution processed spiro-MeOTAD HTL such as pinholes and strong dependence of electrical properties on air exposure, which poses challenges for solar cell stability and reproducibility. In this work, we perform a systematic study to unravel the fundamental mechanisms for the generation of pinholes in solution processed spiro-MeOTAD films. The formation of pinholes is closely related to the presence of small amounts of secondary solvents (e.g., H_2O, 2-methyl-2-butene or amylene employed as stabilizer, absorbed moisture from ambient, etc.), which have low miscibility in the primary solvent generally used to dissolve spiro-MeOTAD (e.g., chlorobenzene). The above findings are not only applicable for spiro-MeOTAD (a small organic molecule), but also applicable to polystyrene (a polymer). The influences of secondary solvents in primary solvents are the main cause for generation of pinholes on film morphology. Our findings are of direct relevance for reproducibility and stability in perovskite solar cells and can be extended to many other spin-coated or drop-cast thin films.

1. Introduction

Lead halide perovskite materials possess a number of attractive properties for photovoltaic applications, such as wide photon absorption wavelength range (~800 nm), small exciton-binding energy (<50 meV), and high carrier mobilities (electron mobility ~ 8 and hole mobility ~ 12 $cm^2/V\ s$) [1, 2]. Current technological challenges (e.g. small cell areas, instabilities, PCE lower than theoretically predicted Shockley-Queisser limit, hysteresis, etc) are closely correlated with fundamental bulk as well as interface properties within a complete solar cell device [3-8]. Following the first few pioneering reports [9-12], optimization of perovskite film preparation and device architecture has led to power conversion efficiencies (PCEs) exceeding 22% [13]. One of the major improvements that allowed

1

higher PCEs as well as prolonged lifetime was the replacement of the liquid electrolyte to solid state 2,2',7,7'-tetrakis(N,N-di-p-methoxyphenylamine)-9,9'-spirobifluorene (spiro-MeOTAD) hole transport layer (HTL) [10, 14, 15]. However, spiro-MeOTAD HTLs deposited using the widely adopted recipe show serious issues such as strong influence of air exposure on conductivity, interface energy level variations [14, 16, 17], crystallization [18], photo-oxidation of spiro-MeOTAD [19], instability (i.e., morphological deformation at high temperature, showing large voids in the spiro-MeOTAD HTL when the devices are heated at 80 °C and above) [20, 21], diffusion of Au or other metal electrode (high incident kinetic energy metal particles) into spiro-MeOTAD [3, 22], and iodization of top electrode due to high temperature [3].

Since 2014, our group together with collaborators has been investigating the physical and chemical properties of spiro-MeOTAD to find the influence of ambient gas exposure and light exposure on solar cell performance and stability [15, 17, 23-28]. It was found that spin-coated spiro-MeOTAD films using chlorobenzene as the solvent exhibited a high density of pinhole population (small sized pinholes ~4 pinholes/μm^2 with an average diameter of ~135 nm and large sized pinholes ~289 pinholes/mm^2 with diameters in the range of 1−20 μm) [24]. Additional cross-sectional view scanning electron microscopy (SEM) measurements revealed that these pinholes form channels wiggling across the film thickness (~240 nm), which were confirmed by a few other groups [29-31]. These pinholes facilitate the inward diffusion of gas molecules present in ambient air (e.g. H_2O and O_2) leading to detrimental effects of the underlying perovskite layer [26]. In addition, these pinholes also facilitate the outward diffusion of chemical elements/compounds with high vapor pressure such as iodine-containing volatile species (e.g., HI, CH_3NH_2, I_2, CH_3I, NH_3) as a result of the degradation of $CH_3NH_3PbI_3$ perovskite films [25, 32]. Moreover, the pinholes in spiro-MeOTAD HTLs cause solar cell efficiency to drop over time [27]. Further systematic investigations were conducted to understand the influences of individual Li-bis(trifluoromethanesulfonyl)-imide (LiTFSI) and 4-*tert*-butylpyridine (*t*-BP) additives on the overall spiro-MeOTAD HTL morphology using chloroform as solvent [33]. The combined 2D Fourier transform IR microscopy and atomic and electrostatic force microscopy (AFM/EFM) study reveals the spatial distribution of spiro-MeOTAD, LiTFSI and *t*-BP that were directly correlated with spatially mapped chemical composition, roughness, and conductivity. Without *t*-BP, incorporation of LiTFSI alone leads to increased amounts of aggregation of LiTFSI, causing an overall rough and inhomogeneous HTL film. In this sense, *t*-BP was essential as plasticizer helping to prevent phase segregation of LiTFSI and spiro-MeOTAD, resulting in a substantially more homogeneous HTL film [33, 34]. Another finding from this study is that pinholes are not induced by the presence of LiTFSI or *t*-BP additives [33]. The influences of these pinholes on perovskite solar cell performance and stability were described in our previous works [15, 17, 23-28]. However, main questions on "how these pinholes are generated? What physico-chemical properties lead to pinhole generation?" were still lacking. In this work, we provide the fundamental physico-chemical aspects of how pinholes are generated.

Interestingly, in our previous publication [27] we found that when spiro-MeOTAD was dissolved in chloroform, pinholes were not generated. This provided us with hints that pinhole generation was strongly influenced by the choice of solvents. In this work, we investigated systematically the influences of several solvents (chlorobenzene, chloroform, dichloromethane, and toluene) with the aim to correlate solvents' physical properties (i.e., molecular weight, density, viscosity, dipole moment. See Table 2) with formation and physical properties of pinholes (i.e., size and density). We show that the formation of pinholes is induced by the presence of a secondary solvent (e.g., water, stabilizer additive) in the primary solvent. Four different solvents (chlorobenzene, chloroform, dichloromethane, and toluene; each solvent was purchased from two companies: Sigma-Aldrich and Wako) were used as primary solvents to dissolve spiro-MeOTAD. Si wafers with a native silicon oxide layer were used as substrates as its flatness, root-mean square (RMS) roughness ~ 0.1 nm, facilitates the visualization and characterization of pinholes by AFM. Previously, we have shown that pinholes are also observed when spiro-MeOTAD is spin-coated on the $CH_3NH_3PbI_3$ perovskite layer, suggesting that pinhole formation has an insignificant dependence on the substrate choice [25, 27] . It has also been observed that the pinhole formation is not mainly caused by LiTFSI and t-BP [33], which are the two common additional constituents in spiro-MeOTAD HTL preparation; pinholes are present on pure spiro-MeOTAD films (i.e., without LiTFSI and t-BP) as well [24]. We conducted a systematic morphology studies of spin-coated spiro-MeOTAD films that were dissolved in four different solvents (chlorobenzene, toluene, chloroform, and dichloromethane). We were not able to establish a direct correlation between generation of pinholes and intrinsic physico-chemical properties (e.g. boiling point, viscosity, dipolar moment strength, polarizability and density) of the solvents that were used [35]. On the other hand, spin-coated spiro-MeOTAD dissolved in chlorobenzene from Sigma-Aldrich showed the presence of pinholes while chlorobenzene from Wako did not generate pinholes. The examination of the product information from these two companies reveals a key difference between these two chlorobenzene products, i.e., the presence of water and/or additives. Specifications of chemical contents in different solvents regarding purity were described in Experimental Section and Table 1. To assess the effects of the small amount of water and/or additives, we conducted control experiments by adding intentionally small amounts of water and 2-methyl-2-butene (amylene). The different amounts of additives are commonly employed to prolong the solvent shelf life (e.g., amylene in dichloromethane), Table 1. It is found that pinhole formation, size, and distribution are strongly influenced by the small amounts of H_2O (named in this work as the secondary solvent), which has low miscibility in the primary solvents (e.g., chlorobenzene, dichloromethane, toluene, or chloroform). Similarly, the amylene additive employed in dichloromethane also generates a large density of pinholes in the spiro-MeOTAD films. The aforementioned findings are not unique to only organic solvents consisting of small organic molecules, and pinholes were also observed when employing polystyrene, a polymer composed of long hydrocarbon chains that serve as a model compound of aromatic HTL, e.g., poly(triaryl amine) (PTAA), poly(3-hexylthiophene) (P3HT), commonly used in perovskite-based solar cells. The influences of

secondary solvents and additives in primary solvents are expected to have a broad range of potential applications and large influence in morphology of the deposited layers.

2. Experimental Section

Table 1. Specification for each of the solvents used in this work.

Solvent	Company and Product Number	Note
Chlorobenzene	Sigma-Aldrich – P/N284513	Anhydrous 99.8%: - Water (by Karl Fischer) ≤ 0.005% - Residue on evaporation ≤ 0.0005%
	Wako – P/N032-07986	Special Grade: - Water: max. 0.03% - Acidity (as HCl): max. 0.01% - Chloride (Cl): max. 1 ppm
Dichloromethane	Sigma-Aldrich – P/N270997	Anhydrous ≥99.8%: - Amylenes as stabilizer: 40 – 150 ppm - Water (by Karl Fischer): ≤ 0.001%
	Wako – P/N042-31231	Super Dehydrated: - Water: max. 0.001% - Residue after evaporation: max. 0.001% - Acidity (as HCl): max. 0.001% - Free chlorine: to pass test (Cl: max. about 1 ppm) - Substances darkened by sulfuric acid: to pass test - Iodine-consuming substances: to pass test (as HCHO: max. about 4 ppm) - Assay (capillary GC): min. 99.5% - 2-Methly-2-butene (stabilizer): 0.0005~0.005%
Toluene	Sigma-Aldrich – P/N244511	Anhydrous 99.8%: - Residue on evaporation: ≤ 0.0005% - Water (by Karl Fischer): ≤ 0.001%
	Wako – P/N202-17911	Super Dehydrated: - Water: max. 0.001% - Acidity (as HCl): max. 0.001% - Alkalinity (as NaOH): max. 0.001% - Sulfur compounds: to pass test (as S: max. about 6 ppm) - Thiophene: to pass test (C_4H_4S: max. about 1 ppm) - Substances darkened by sulfuric acid: to pass test - Assay (capillary GC): min. 99.5%
Chloroform	Wako – P/N032-21921	Super Dehydrated:

		- Water: max. 0.001%
		- Residue after evaporation: max. 0.001%
		- Acidity (as HCl): max. 0.001%
		- Chloride (Cl): max. 1 ppm
		- Free chlorine: to pass test (Cl: max. about 1 ppm)
		- Carbonyl compounds (as CO): max. 0.005%
		- Carbon tetrachloride (CCl_4): max. 0.01%
		- Substances darkened by sulfuric acid: to pass test
		- Suitability for use with dithizone: to pass test
		- Assay (capillary GC): min. 99.0%
		- Ethanol (stabilizer): 0.3~1.0%

Preparation of primary solvents. 72.5 mg of spiro-MeOTAD (SunaTech Inc. and SHT-263 Merck Livilux) was dissolved in 1 mL of four different solvents (chlorobenzene, chloroform, dichloromethane, and toluene), which corresponds to concentration of 59.2 mM. Unless stated otherwise spiro-MeOTAD from SunaTech Inc. was employed throughout this work. 60 µL of solution was spin-coated at 2000 rpm for 60 s on Si substrates (~1x1 cm^2). AFM (MFP-3D series, Asylum Research) was used to characterize films' morphologies. As-received Si(100) wafers covered with native silicon oxide (SAMCO Inc., 0.013 Ω·cm) were used as substrates. Except for the companies from which the solvents were purchased, the organic layer deposition follows identical procedure. From Sigma-Aldrich chlorobenzene anhydrous 99.8% (284513), dichloromethane anhydrous >99.8%, 40-150 ppm amylene as stabilizer (270997), and toluene anhydrous 99.8% (244511) were tested. From Wako, chlorobenzene Mono (032-07986), dichloromethane super dehydrated (042-31231), toluene super dehydrated (202-17911), chloroform (038-18495) and chloroform super dehydrated (032-21921) were tested. We extract the relevant information from the datasheets of these solvents, which is summarized in Table 1. The film thicknesses determination was conducted using AFM by mapping the height differences in a region of spiro-MeOTAD film with a thin scratch made with the aid of a surgical stainless steel blade (Kai medical, 322-B). The histograms shown in figure 4 were generated using Gwyddion 2.41 modular program for scanning probe microscopy (SPM) data visualization and analysis. More information can be found at *gwyddion.net*. The modules "Mark Grains by Threshold" and "Grain Distributions" were used. Adjusting manually the threshold level, which corresponds to the height (plane) in AFM images, in the "Mark Grains by Threshold" module, it is possible to mask all the areas corresponding to the pinholes. The flatness of the substrate is important to accurately obtain all the pinholes masked. In the subsequent step, the "Grain Distributions" module is evoked, which generates histograms with several relevant physical parameters. The same systematic tests described for spiro-MeOTAD molecules were

also performed with polystyrene (PS, Sigma-Aldrich 441147, average Mw ~ 350,000, average Mn ~ 170,000). 32.4 mg of PS was dissolved in 2 mL of solvent.

Preparation of solutions with secondary solvents in the primary solvents. Systematic studies of intentional addition of small amounts of secondary solvents were performed using deionized water (Millipore, >18 MΩ·cm) and 2-methyl-2-butene (amylene, >99% purified by redistillation, Sigma-Aldrich M32704-100ML).

3. Results and Discussion

3.1. Identification of solvents leading to pinhole generation.

Table 2. Physico-chemical properties of chlorobenzene, toluene, chloroform, and dichloromethane non-polar solvents. [a]As comparison, the specific gravity and dipole moment of H_2O is 1 and 1.85 D, respectively.
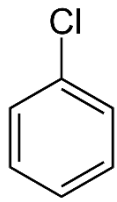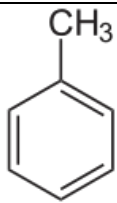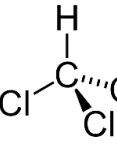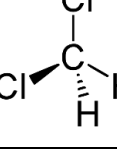
Solvent	Molecular structure	Boiling point at 1 atm (˚C)	Molecular weight (g/mol)	Density at 25 ˚C (g/mL)	Viscosity at 25 ˚C (mPa·s)	Dipole moment (D)
Chlorobenzene (C_6H_5Cl)		132	112.56	1.11	0.753	1.54
Toluene (C_7H_8)		111	92.14	0.86	0.590	0.36
Chloroform ($CHCl_3$)		61.2	119.38	1.49	0.542	1.04
Dichloromethane (CH_2Cl_2)		39.6	84.93	1.33	0.413	1.60

6

Figure 1 shows the AFM topography images of three samples of undoped spiro-MeOTAD films using chlorobenzene, dichloromethane, and toluene solvents (all purchased from Sigma-Aldrich) and spin-coated on Si substrates, respectively. Detailed sample preparation conditions can be found in the experimental section. Large variations in pinhole density and sizes were observed according to the solvents used to dissolve spiro-MeOTAD. As it will be described below, although the spiro-MeOTAD film thickness is strongly affected by intrinsic physico-chemical properties (especially boiling point) of the different solvents (Table 2) [33], the pinhole formation is not. We have limited in providing quantitative analysis of pinhole density and size of spin-coated films with spiro-MeOTAD dissolved in different solvents because the pinhole formation does not depend on solvent physico-chemical properties. We find that pinhole formation and its properties (size and distribution) depend on solvents purity that can vary according to the specified grade, the storage time, and/or impurities introduced by solutes. Furthermore, we found that the formation of pinholes was closely related to the presence of secondary solvents (e.g., water and / or additives) in the primary solvent (chlorobenzene, dichloromethane, and toluene).

In figure 2, another set of samples were prepared by dissolving spiro-MeOTAD in the same type of solvent (chlorobenzene, dichloromethane, and toluene) but purchased from a different company Wako. In addition, chloroform (Wako), which is another widely used solvent was tested in our studies. figure 2 shows that the degree of pinhole formation is significantly reduced. As indicated in figure 2 caption, surface roughness RMS of (a) 0.22 nm and (b) 0.20 nm with chlorobenzene; (c) 0.21 nm and (d) 0.23 nm with dichloromethane; (e) 0.22 nm and (f) 0.21 nm with toluene; (g) 0.19 nm and (h) 0.18 nm with chloroform were extracted when spiro-MeOTAD dissolved in different solvents was deposited on silicon substrates. A statistical analysis taking into account all values above leads to 0.21 ± 0.02 nm as average surface roughness RMS, where the small standard deviation of 0.02 nm indicates a small variability of the roughness from its mean value. Therefore, we find that spiro-MeOTAD film roughness is uncorrelated with the different solvents employed in this study. As comparison, RMS of 0.12 ± 0.02 nm were previously reported for vacuum-prepared undoped spiro-MeOTAD films on Si substrates meaning that similar film morphology was obtained for both methods [23, 26]. Photographs of the spiro-MeOTAD films on Si substrates were shown in the insets. Discernible color differences were observed among four samples, which was attributed to differences in thickness of films [36]. Typical thicknesses of 190 ± 5 nm, 265 ± 5 nm, 367 ± 13 nm, and 402 ± 14 nm were extracted when spiro-MeOTAD was spin-coated from chlorobenzene, toluene, chloroform, and dichloromethane, respectively (Table 3). The obtained thicknesses were observed to correlate directly with boiling points (T_B) of solvents (Table 2). The dichloromethane solvent, which has the lowest T_B of 39.6 ˚C, generated the thickest spiro-MeOTAD film (thickness ~ 400 nm) while the chlorobenzene solvent with the highest T_B of 132 ˚C produced the thinnest film (thickness ~ 190 nm).
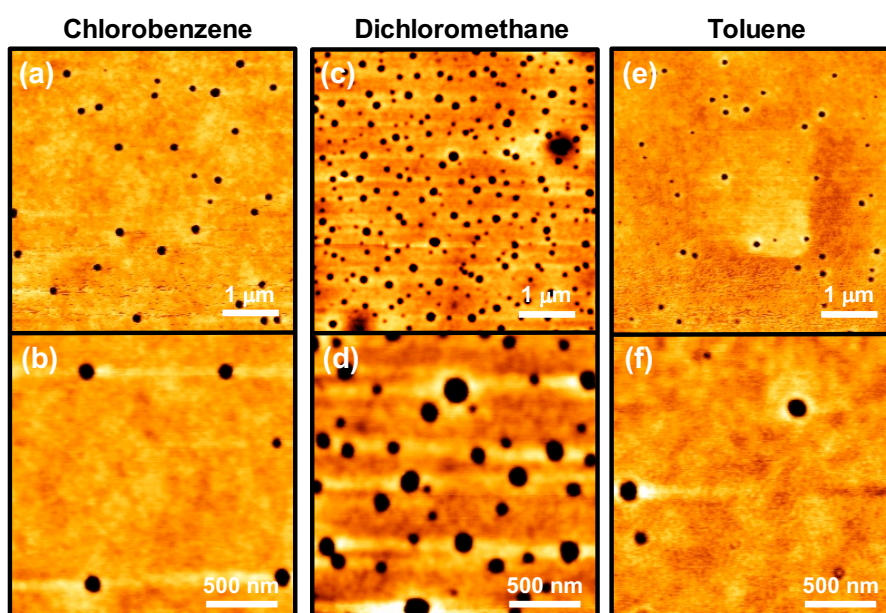
Figure 1. High density of pinholes in spin-coated spiro-MeOTAD films in presence of secondary solvents. Tapping mode AFM topography images (a,c,e) 5x5 μm^2 and (b,d,f) 1×1 μm^2 of spin-coated spiro-MeOTAD films on Si substrates using Sigma-Aldrich (a,c) chlorobenzene, (c,d) dichloromethane, and (e,f) toluene.
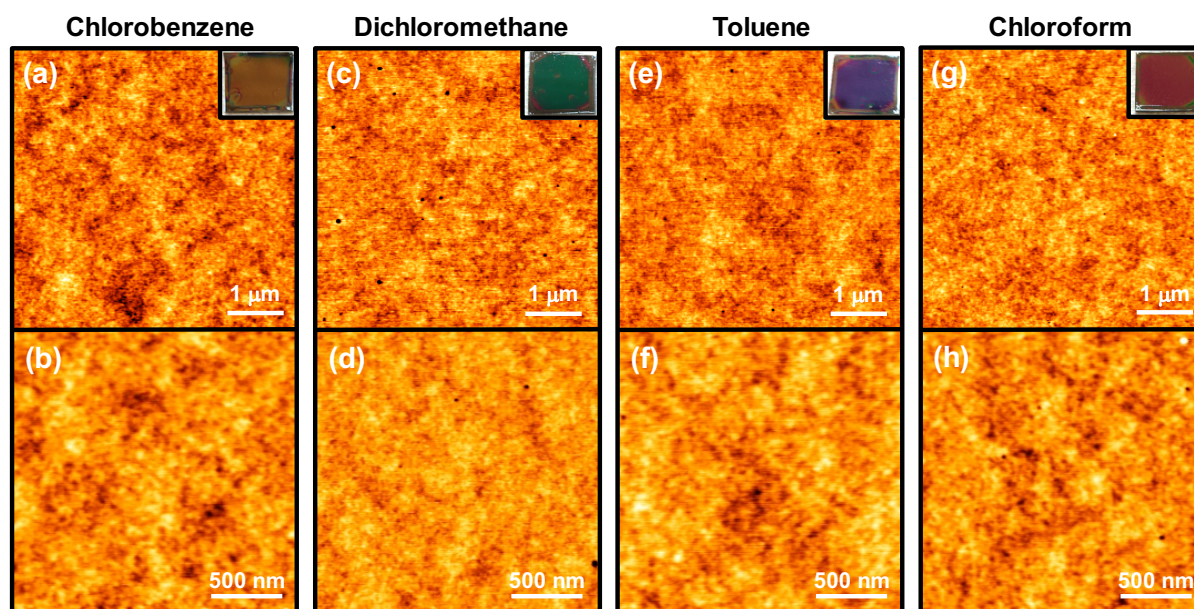

Figure 2. Pinholes free spiro-MeOTAD films in the absence of secondary solvents. Tapping mode AFM topography images (a,c,e,g) 5x5 μm^2 and (b,d,f,h) 1x1 μm^2 of spin-coated spiro-MeOTAD films on Si substrates using Wako (a,c) chlorobenzene, (c,d) dichloromethane, (e,f) toluene, (g,h) chloroform. Surface roughness root-mean square of (a) 0.22 nm, (b) 0.20 nm, (c) 0.21 nm, (d) 0.23 nm, (e) 0.22 nm, (f) 0.21 nm, (g) 0.19 nm, and (h) 0.18 nm were extracted. Pictures of the samples are shown in the insets.

3.2. Presence of secondary solvent in the primary solvent leads to pinhole generation.

A correlation was not found between pinhole formation and solvent intrinsic physico-chemical properties. A comparison between the two sets of solvent products (figures 1 and 2) is made regarding the presence of water and/or additives (i.e., secondary solvents) in different amounts in the primary solvents specified by the companies. A summary of the additives and other impurities can be found in Table 1. Our hypothesis is that the presence of this secondary solvent in the primary solvent is the cause for the pinholes formation. In some primary solvents, stabilizers are added to prolong shelf lifetime. As an example, amylene in different amounts (depending on companies' specification; Table 1) are added in dichloromethane. Furthermore, spin-coated spiro-MeOTAD films employing dichloromethane from both companies revealed that the density of generated pinholes (figure 1c,d and figure 2c,d) may be correlated with the amounts of additive (Table 1). To test this hypothesis, we performed a control experiment by intentionally adding small amounts of water in the primary solvents. Figures 3(a-d) show spiro-MeOTAD film surface morphology after addition of 1 vol.% and 5 vol.% of deionized water (DI-H_2O, Millipore, >18 MΩ·cm) in the primary solvents of chlorobenzene and dichloromethane. Size distribution analyses based on AFM images are shown in figures 4(a-d). Spin-coated spiro-MeOTAD films using chlorobenzene solvent with 1 vol.% and 5 vol.% of DI-H_2O, generated pinholes with average sizes of 93 ± 79 nm and 118 ± 103 nm, respectively. On the other hand, adding same amounts of 1 vol.% and 5 vol.% of DI-H_2O in chloroform generated much smaller sizes of pinholes with average diameters of 45 ± 17 nm and 44 ± 18 nm, respectively (Table 3). As displayed in the raw AFM images (figure 3a,b), when H_2O is added into chlorobenzene solvent, it leads to a broader size distribution in pinhole diameters (Figures 4a,b), which shows that the standard deviation is comparable to the mean pinhole size. The statistical origin for this is due to the formation of pinholes with at least two distinct size distributions (i.e. bimodal distribution), which leads to a high standard deviation indicating that the data points are widely spread out (Figures 3a,b and 4a,b; chlorobenzene case). The fundamental physico-chemical properties leading to this bimodal distribution in pinhole size distribution is challenging to be unraveled at the current stage of our research. Further detailed experimental procedure would be needed to determine (1) what are the constituents of the secondary solvents that comes in the primary solvents? (2) determine the fundamental interaction mechanisms between primary solvent and secondary solvent with spiro-MeOTAD; (3) what physico-chemical properties lead to pinhole generation? In addition to the manufacturing company (e.g., Wako or Sigma-Aldrich), lot-to-lot (i.e., bottle-to-bottle variations from the same company) and shelf-storage time were also observed to influence on the pinhole size distribution. I.e., the concentration of these secondary solvents varies according to bottle-to-bottle and shelf-storage time. Therefore, tracking the physico-chemical origins that leads to differences in pinhole size is challenging.

We also considered adding intentionally small amounts of amylene, which is a well-known stabilizing additive to extend product shelf life of chloroform and dichloromethane [37]. Figures 3e,f show AFM topography images of the spiro-MeOTAD films prepared using chloroform (Wako, 032-21921) to which different amounts of amylene (M32704-100ML, Sigma-Aldrich) was added. When amylene was added, pinholes started to appear. Statistical analyses on pinhole density and size distribution were conducted to obtain a comprehensive understanding about influences of amylene (figures 4e,f). Spin-coated spiro-MeOTAD films using the chloroform solvent with 5 vol.% and 20 vol.% of amylene, generated pinholes with average sizes of 42 ± 9 nm and 68 ± 21 nm, respectively (Table 3).

Table 3. Summary of generated pinholes densities and diameters as a function of different controlled amounts of secondary solvents in the primary solvents. Solvents purchased from Wako was employed in this study.

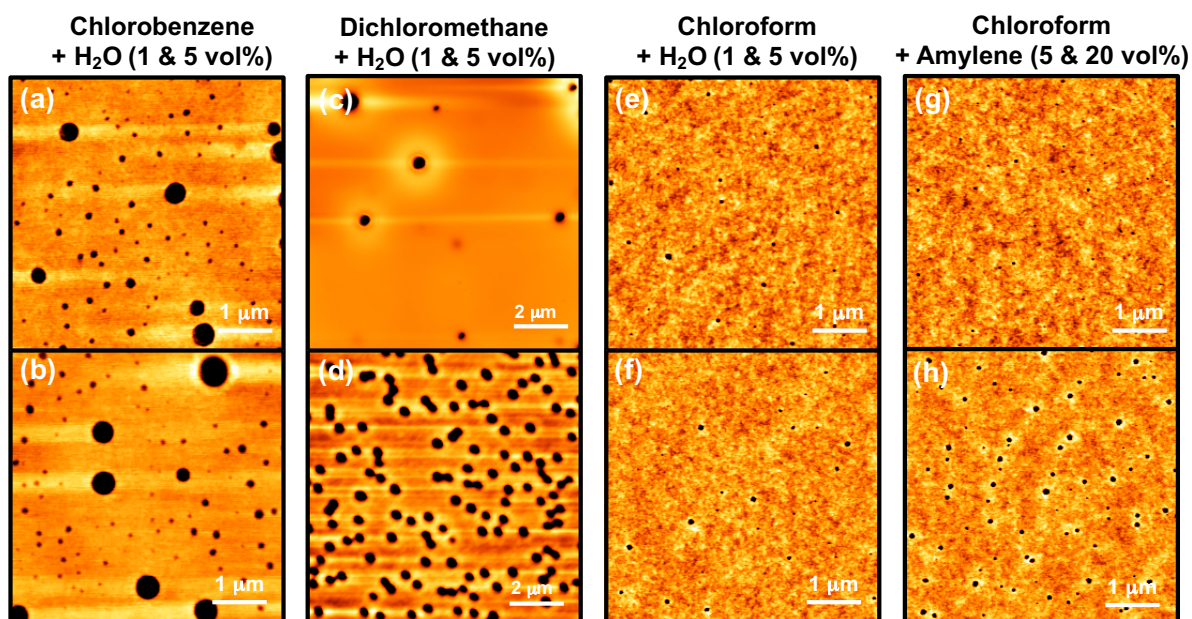| Solvent	Pinhole density (μm^{-2})	Average diameter (nm)
Chlorobenzene (1 vol% H_2O)	69	93 ± 79
Chlorobenzene (5 vol% H_2O)	83	118 ± 103
Dichloromethane (1 vol% H_2O)	41	273 ± 124
Dichloromethane (5 vol% H_2O)	59	345 ± 89
Chloroform (1 vol% H_2O)	93	45 ± 17
Chloroform (5 vol% H_2O)	99	44 ± 18
Chloroform (5 vol% amylene)	34	42 ± 9
Chloroform (20 vol% amylene)	86	68 ± 21

Figure 3. Spin-coated spiro-MeOTAD topography with controlled amounts of water and amylene as secondary solvent. Tapping mode AFM topography images (5x5 μm^2) of spin-coated spiro-MeOTAD films using Sigma-Aldrich chlorobenzene to which (a) 1 vol% and (b) 5 vol% of deionized water were added. Similarly, dichloromethane from Wako to which (c) 1 vol% and (d) 5 vol% of deionized water. Chloroform from Wako to which (e) 1 vol% and (f) 5 vol% of deionized water as well as (g) 5 vol% and (h) 20 vol% of amylene were added and spin-coated on Si substrates.
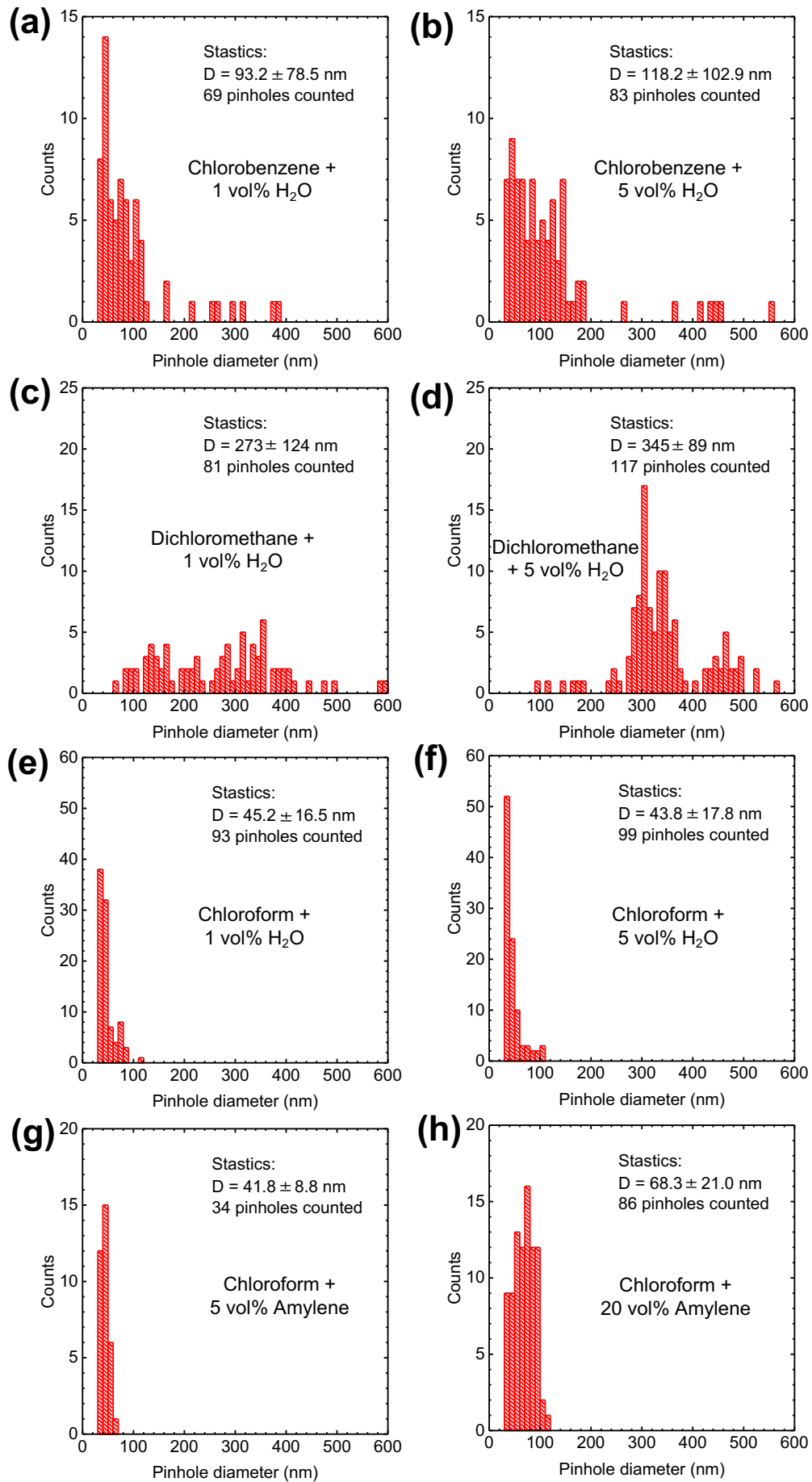
(a)
Stastics:
D = 93.2 ± 78.5 nm
69 pinholes counted

Chlorobenzene +
1 vol% H_2O

(b)
Stastics:
D = 118.2 ± 102.9 nm
83 pinholes counted

Chlorobenzene +
5 vol% H_2O

(c)
Stastics:
D = 273 ± 124 nm
81 pinholes counted

Dichloromethane +
1 vol% H_2O

(d)
Stastics:
D = 345 ± 89 nm
117 pinholes counted

Dichloromethane
+ 5 vol% H_2O

(e)
Stastics:
D = 45.2 ± 16.5 nm
93 pinholes counted

Chloroform +
1 vol% H_2O

(f)
Stastics:
D = 43.8 ± 17.8 nm
99 pinholes counted

Chloroform +
5 vol% H_2O

(g)
Stastics:
D = 41.8 ± 8.8 nm
34 pinholes counted

Chloroform +
5 vol% Amylene

(h)
Stastics:
D = 68.3 ± 21.0 nm
86 pinholes counted

Chloroform +
20 vol% Amylene

12

Figure 4. Histograms showing the distribution of pinhole diameters when secondary solvents of H_2O and Amylene are added intentionally in the primary solvents of chlorobenzene, dichloromethane and chloroform. The statistical analyses are based on the AFM images (5x5 μm^2) shown in figure 3.

3.3. Spiro-MeOTAD film morphology when deposited on perovskite films.

We conducted additional experiments to study the influences of secondary solvents on the morphology of spiro-MeOTAD films spin-coated on perovskite films. In our previous works shown in figure S6 in ref. [25] and figure 1a,b in ref. [27], we observed pinholes when LiTFSI and *t*-BP doped spiro-MeOTAD were spin coated on solution processed $CH_3NH_3PbI_3$ perovskite films. In this work, we conducted morphological characterization of pinholes induced by the secondary solvents in undoped spiro-MeOTAD films when spin coated on $CH_3NH_3PbI_3$ films prepared by CVD [38-41]. $CH_3NH_3PbI_3$ films prepared by this method are smooth with low surface roughness that facilitates detection and analysis of pinhole properties such as densities and sizes (figure 5a,b). Furthermore, the new experiments provide insight on the spiro-MeOTAD film morphology when spin coated on $CH_3NH_3PbI_3$ perovskite films by a vapor based dry process.
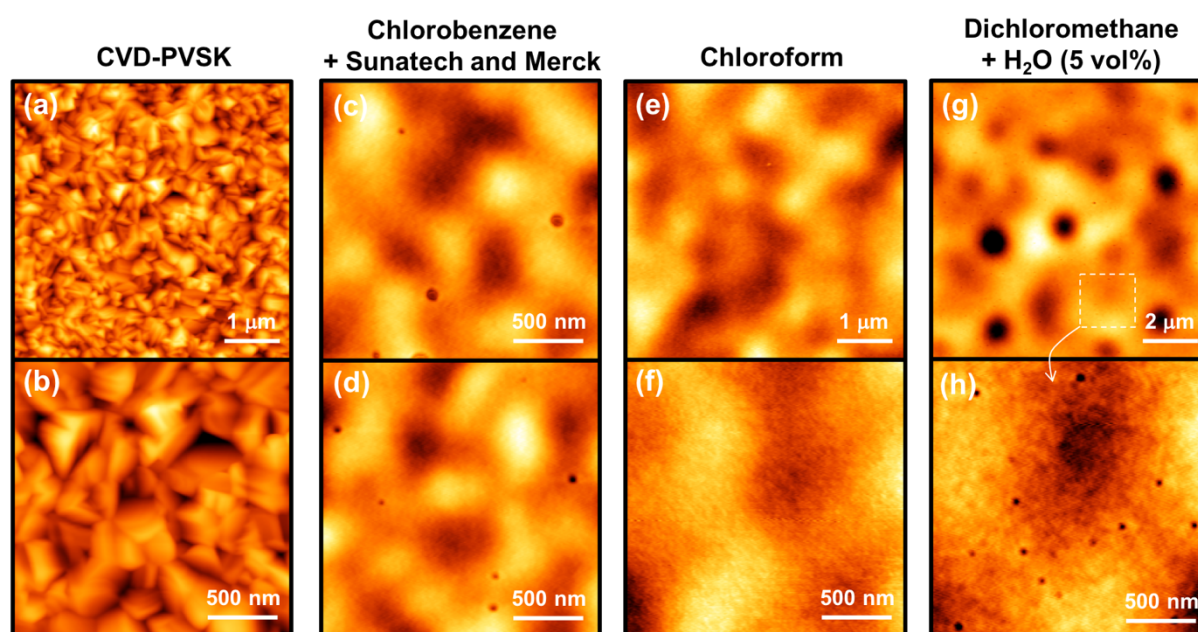

Figure 5. Tapping mode AFM topography images (a) 5×5 μm^2 and (a) 2×2 μm^2 of glass/FTO/c-TiO$_2$/CH$_3$NH$_3$PbI$_3$ with perovskite films prepared by the CVD method. Surface roughness root-mean-square of 27 nm was extracted on both images. (c,d) 2×2 μm^2 of glass/FTO/c-TiO$_2$/CH$_3$NH$_3$PbI$_3$/spiro-MeOTAD using chlorobenzene from Sigma-Aldrich to dissolve spiro-MeOTAD purchased from two companies: (c) Sunatech Inc. and (d) Merck Livilux. (e) 5×5 μm^2 and (f) 2×2 μm^2 of glass/FTO/c-TiO$_2$/CH$_3$NH$_3$PbI$_3$/spiro-MeOTAD using chloroform from Wako to dissolve spiro-MeOTAD. (g) 5×5 μm^2 and (h) 2×2 μm^2 of glass/FTO/c-TiO$_2$/CH$_3$NH$_3$PbI$_3$/spiro-MeOTAD using spiro-MeOTAD in

dichloromethane from Sigma-Aldrich with 5 vol% deionized H_2O. Surface roughness root-mean-square of (c) 2.2 nm, (d) 2.3 nm, (e) 1.9 nm, (f) 1.1 nm, (g) 2.6 nm, (h) 0.7 nm were extracted.

Figure 5a,b shows the AFM topography images of the perovskite films prepared by the CVD method. A detailed description of CVD method to prepare perovskite films are found in our previous works [38-41]. On the basis of the AFM images, we determine the surface RMS roughness of ~27 nm is extracted. As shown in figure 1, when chlorobenzene solvent purchased from Sigma-Aldrich was used to dissolve spiro-MeOTAD, pinholes are generated after spin coating on flat substrates of silicon. Similarly, as shown in figure 5c,d, pinholes are also observed on the CVD grown $CH_3NH_3PbI_3$ films with pinhole size and density suggesting that pinhole formation is only weakly dependent on the type of the substrate [25, 27]. Three locations on the same sample (center, one side of the corner, and opposite corner) were measured to verify that there is no influence of centrifugal forces on pinhole formation during spin coating (not shown). For comparison purposes, we have also employed the chloroform solvent purchased from Wako and it confirms again that pinholes are not observed when spin coated on $CH_3NH_3PbI_3$ perovskite films when using Wako solvents (figure 5e,f) [27]. The presence of pinholes in spiro-MeOTAD hole transport layers has been reported to be detrimental for stability of perovskite solar cells [24]. The pinholes in the previous study [24] were most likely a result of stabilizer (secondary solvent) in the primary solvent (chlorobenzene) used to dissolve spiro-MeOTAD. In the next step, we employ the strategy of intentionally adding controlled amounts of deionized-H_2O as secondary solvents for controlling pinhole size (figures 3 and 4). Dichloromethane was used as primary solvent and controlled amounts of deionized H_2O as secondary solvent was able to generate a high density of pinholes (figure 3c,d). Figure 5g,h shows the new results when spiro-MeOTAD dissolved in dichloromethane with 5 vol% H_2O is spin coated on perovskite film. The AFM images reveal that larger pinholes with sizes ranging from 700 to 900 nm are formed due to addition of H_2O (figure 5g). However, further careful characterization of high-resolution AFM images show that pinholes with smaller sizes are also formed with sizes of ~40 nm (figure 5h). More importantly, the intentionally added H_2O leads to degradation of the perovskite layer indicated by yellow spots formed on the film observed by a visual inspection, i.e., the secondary solvent (H_2O) in direct contact with perovskite generates degraded spots compromising device performance and stability. The example above is an exaggerated condition aiming at generating larger pinholes; however, not suitable for device studies as perovskite films show already degraded surfaces by incorporation of H_2O in the primary solvents. This exemplifies that not only minutes amounts of H_2O, but also solvent stabilizer additives as secondary solvents may have large impact on device performance and stability. We have tested the influence of amylene (added as stabilizer in dichloromethane solvent) on the perovskite film by drop casting directly amylene on the perovskite film inside a N_2 glove box. Although no color changes were observed by a visual inspection, further detailed characterization (e.g., X-ray photoelectron spectroscopy) is needed to draw a conclusion of the influences of amylene on perovskite films. We have re-evaluated the experimental importance,

and its complexity requires a thorough experimental planning such as (1) how to deconvolute the influences of pinhole size and density from the secondary solvent influences on perovskite films and consequently on macroscopic parameters of overall solar cell efficiency and stability; (2) how to determine the chemical compounds present as secondary solvents in the different solvents studied in this work; (3) how these secondary solvents impact the perovskite layer. Considering the facts above, we are planning to elaborate a follow-up work focusing on the topic of the influences of these pinholes that need to be discerned from the direct influences of secondary solvents on the perovskite layer. The influences of the presence of pinholes generated using "pristine" solvents (i.e., without further addition of secondary solvents) on perovskite-based solar cell device performance and stability were described in our previous works [25-27]. We highlight our findings of the influences of pinholes on device efficiency and stability: (1) Regarding device efficiency, similar steady-state or stabilized PCEs are achieved when comparing the $CH_3NH_3PbI_3$-based solar cells with pinholes (i.e., employing chlorobenzene) and without pinholes (i.e., employing chloroform) in the spiro-MeOTAD HTL [27]. It is often a common practice to expose to air for a few hours the freshly spin coated spiro-MeOTAD HTL before Au electrode coating to increase PCE of the perovskite solar cells. Interestingly, we reported that a longer air exposure (or light-soaking) time is necessary to attain maximum PCE in the pinhole-free devices. I.e., the presence of pinholes was observed to help attain maximum PCE in a shorter time during the initial light-soaking on a freshly prepared device [27]. (2) Often these transient behaviors in PCE in perovskite-based solar cells were attributed to the physico-chemical properties and dynamics of the perovskite layer. In addition to the transient behaviors originated from the perovskite layer itself, we have also demonstrated that the spiro-MeOTAD HTL suffers from the variations in the conductivity and hole mobility as a function of air exposure time [17, 24]. The origin for these electrical property changes in HTL were attributed to migration processes of LiTFSI dopant within the spiro-MeOTAD film. Furthermore, this segregation phenomenon was observed to correlate with the morphological properties of solution-processed spiro-MeOTAD films [17, 24]. (3) Regarding $CH_3NH_3PbI_3$ perovskite-based solar cell stability, the presence of pinholes were directly correlated with device efficiency drop over time under storage [25, 26] and operated under maximum power tracking [27]. The stability profile of the pinhole-free cells (using chloroform as solvent) outperformed the cells containing pinholes (using chlorobenzene as solvent) by 10-fold under operation conditions (i.e., under continuous illumination with AM1.5G and applied bias tracking maximum power point) [27]. The device instability was pinpointed to be originated from these pinholes that have the form of channels wiggling across the film thickness, which was visualized by cross-sectional SEM measurements [24]. These pinholes facilitate the inward diffusion of gas molecules present in ambient air (e.g., H_2O and O_2) leading to detrimental effects on the underlying perovskite layer [26, 27]. As consequence, these pinholes also facilitate the outward diffusion of chemical elements/compounds with high vapor pressure such as iodine-containing volatile species (e.g., HI, CH_3NH_2, I_2, CH_3I, NH_3) resulted from the degradation of $CH_3NH_3PbI_3$ perovskite films [25, 32, 42]. Based on the observation above, we have also provided explanation of

why perovskite solar cells employing silver as top-electrode suffers faster degradation. It is commonly observed that silver electrodes turn yellow after device fabrication, which is accompanied by a decrease in PCE. These changes are caused by the formation of silver iodide from the reaction between iodine-containing compounds released from the perovskite decomposition that reaches the silver electrode. Furthermore, the presence of pinholes in spiro-MeOTAD films facilitates the silver iodide formation [25].

3.4. Film morphology of polystyrene in the presence of secondary solvents.

To verify if the characteristic formation of pinholes induced by the secondary solvent is beyond small organic molecules, similar experiments were conducted with polystyrene, an aromatic polymer used in this work as the model material of polymer based HTL. Figure 6 shows that pinhole formation is suppressed when employing the same solvents from Wako. Photographs of the polystyrene films deposited on Si substrates are shown in the insets. Similar to spiro-MeOTAD films, discernible color differences are observed. Thicknesses of 76 ± 2 nm, 205 ± 10 nm, 110 ± 10 nm, and 143 ± 6 nm were extracted when polystyrene was spin-coated using the solvent of chlorobenzene, dichloromethane, toluene, and chloroform, respectively (Table 3). Once again the trends in the thicknesses correlates with T_B, and the solvent with the lowest T_B (dichloromethane) generated the thickest polystyrene film, whilst the solvent with the highest T_B (chlorobenzene) generated the thinnest film. When polystyrene film was dissolved in chlorobenzene from Sigma-Aldrich pinholes were generated (figure 7).
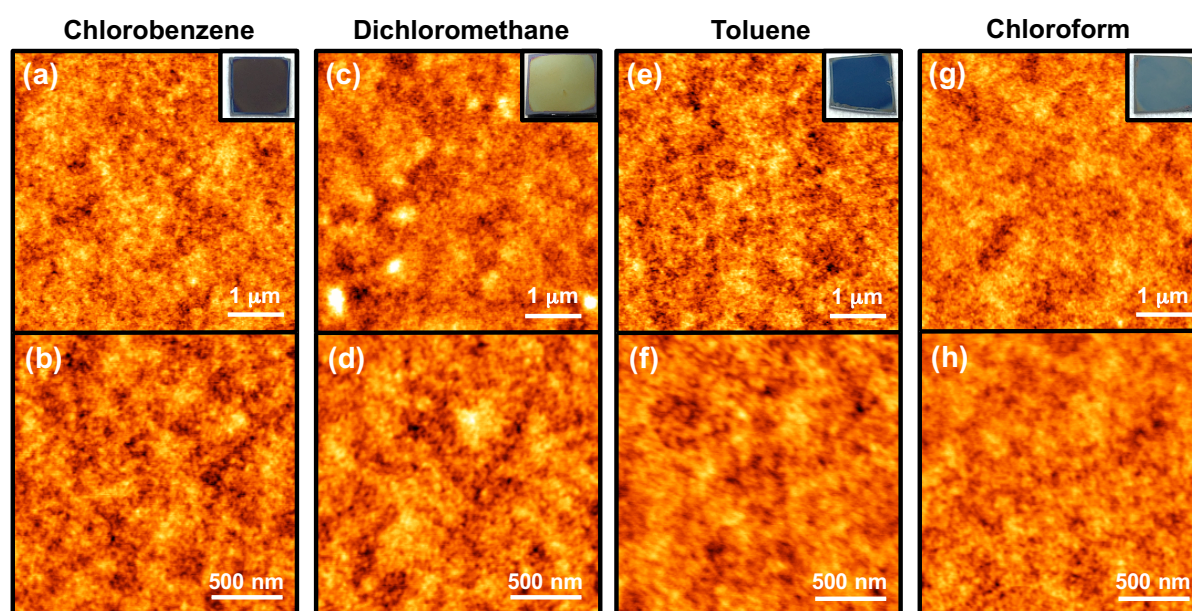

Figure 6. Pinholes free spin-coated polystyrene in absence of secondary solvents.Tapping mode AFM topography images (a,c,e,g) 5x5 μm^2 and (b,d,f,h) 1x1 μm^2 of spin-coated polystyrene films on Si substrates using Wako (a,c) chlorobenzene, (c,d) dichloromethane, (e,f) toluene, (g,h) chloroform.

Pictures of the samples are shown in the insets. Surface roughness root-mean square of (a) 0.22 nm, (b) 0.21 nm, (c) 0.28 nm, (d) 0.20 nm, (e) 0.19 nm, (f) 0.19 nm, (g) 0.20 nm, and (h) 0.17 nm were extracted.

Table 3. Summary of final film thicknesses of spiro-MeOTAD (figure 2) and polystyrene (figure 6) as a function of different employed solvents. Solvents purchased from Wako was employed in this study.

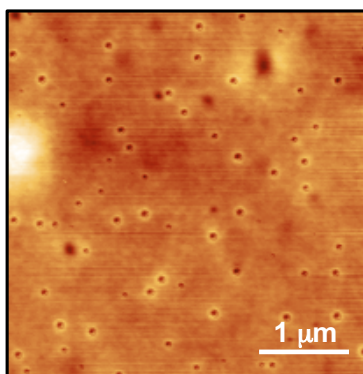| Solvent	Spiro-MeOTAD thickness (nm)	Polystyrene thickness (nm)
Chlorobenzene (T_B = 132 ˚C)	190 ± 5	76 ± 2
Toluene (T_B = 111 ˚C)	265 ± 5	110 ± 10
Chloroform (T_B = 61.2 ˚C)	367 ± 13	143 ± 6
Dichloromethane (T_B = 39.6 ˚C)	402 ± 14	205 ± 10

Figure 7. High density of pinholes in spin-coated polystyrene in the presence of secondary solvents. Tapping mode AFM topography images (5x5 μm^2) of spin-coated polystyrene films using chlorobenzene from Sigma-Aldrich. Si was used as substrates.

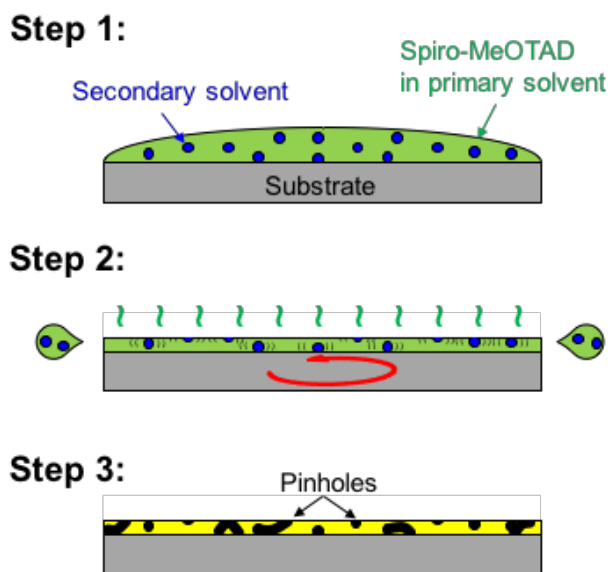**Step 1:**

Step 2:

Step 3:

Figure 8. Schematic illustration of a proposed mechanism for wiggling pinhole channels in spiro-MeOTAD films when secondary solvents (e.g. H_2O) are contained in the primary solvents.

The mechanisms for the pinhole formation is proposed in figure 8. In this model it is not possible to provide mathematical formulations that is based on physico-chemical relevant parameters of solvents as fitting parameters. As shown in Table 2, we studied the correlations between solvents' physical properties (i.e., molecular weight, density, viscosity, dipole moment) and formation as well as physical properties of pinholes (i.e., size and density) by systematically investigating the influences of different solvents (chlorobenzene, chloroform, dichloromethane, and toluene). However, a correlation was not found between pinhole formation and physical properties of solvents. A careful comparison between the solvents are made regarding the presence of water, additives, and/or other impurities (i.e., secondary solvents) in different amounts in the primary solvents specified by the company (Table 1). we succeeded in confirming this hypothesis by adding intentionally small amounts of H_2O and amylene additives in the primary solvents. These were described in sections 3.2. and 3.3. Qualitatively, it has been described that the nature of solvents such as the boiling point, dipole moment, viscosity, solubility of materials, spin-steps, spin-rate affect the crystallinity and morphology of the prepared film [35, 43-47]. For example, it has been pointed out previously that pinholes can form as a result of localized dewetting or microbubbles formed from degassing during the film drying process [45, 46]. Localized dewetting can be caused by contaminants such as dust particles in the air or impurities in solvents. However, in our study we show that pinhole formation is mainly caused by the presence of a secondary solvent that has low solubility for organic solute compared to the primary solvent used to dissolve the solute material (Step 1, figure 8). When the substrate starts to spin, the coating material spreads over the substrate by centrifugal forces. Eventually, the excess solution will fly away leaving the substrate with the amount of solution that can adhere to the substrate (Step 2, figure 8) [35, 48]. During the

spinning of the substrate the complex physico-chemical dynamic processes of the secondary solvent incorporated in the primary solvent are expected to generate not only simple pinholes formed on top surface of spiro-MeOTAD, but also the more complex wiggling channels within the film (Step 3, figure 8) [24, 29-31, 35]. Theoretical models for predicting the film thickness as a function of various spin-coating processing parameters were developed to a high degree of accuracy [49-51]. However, the molecular-level structure and properties of the resulting solid films are difficult to be predicted based on the spin-coating processes because of the complexity of many parameters to be considered (in addition to the parameters shown in Tables 1 and 2, our proposed model of secondary solvents in the primary solvent needs to be taken into account) and the dynamics of physico-chemical mechanisms involved during sample spinning [48, 52]. As pointed out in several works, the effects of the spin-coating processing conditions on the film morphology such as crystallization/ordering, aggregation, phase-segregation phenomena, as well as performance evaluation in organic electronic devices are mainly tested empirically [51, 53-60]. Our proposed model in figure 8 is in line with the study of pinhole observation in polymethylmethacrylate (PMMA) reported by Semaltiamos et al. [61]. The formation of pinholes in PMMA were proposed to be accompanied by the additional removal (evaporation) of the excess trapped solvent from the film. These results indicate that spin-coated films are not in a complete dry state but rather contain a certain amount of solvents [20, 21, 61].

4. Conclusions

Spin-coating is generally employed as an easy and fast method for the thin-film preparation. However, when spiro-MeOTAD (a widely used hole transport materials in lead halide perovskite solar cells) is dissolved in a certain primary solvent, pinholes are observed on spin-coated films. Our systematic study employing chlorobenzene, chloroform, dichloromethane, and toluene as primary solvents as well as H_2O and amylene as secondary solvents confirms that the main factor for generation of pinholes in model HTL are (i) presence of a secondary solvent in the primary solvent and (ii) considerable miscibility variations between primary and secondary solvents. Furthermore, it is found that this mechanism is not only applicable for spiro-MeOTAD (a small organic molecule), but also applicable to polystyrene (an aromatic polymer compound used as model material for polymer based HTL.). Our systematic study shows how a precise control of the secondary solvents in precursor solutions of spin-coated small organic molecules or polymers results in high reproducibility of HTL film morphology that affects device efficiency and stability.

Authors contributions

Y.B.Q. conceived the idea, initiated, and supervised the work. L.K.O. prepared the samples and performed the AFM experiments. Z.H. and E.J.J.P. gave valuable suggestions to this work. L.Q. and Y.J. prepared the perovskite films grown by CVD. All authors contributed to writting the manuscript.

References

[1]   Grätzel M 2014 The light and shade of perovskite solar cells *Nature Mater.* **13** 838-42
[2]   D'Innocenzo V, Grancini G, Alcocer M J, Kandada A R, Stranks S D, Lee M M, Lanzani G, Snaith H J and Petrozza A 2014 Excitons versus free charges in organo-lead tri-halide perovskites *Nat. Commun.* **5** 3586
[3]   Lei L, Zhang S, Yang S, Li X, Yu Y, Wei Q, Ni Z and Li M 2018 Influence of hole transport material/metal contact interface on perovskite solar cells *Nanotechnology* **29** 255201
[4]   Suzuki A, Kida T, Takagi T and Oku T 2016 Effects of hole-transporting layers of perovskite-based solar cells *Jpn. J. Appl. Phys.* **55** 02BF1
[5]   Ye M, He C, Iocozzia J, Liu X, Cui X, Meng X, Rager M, Hong X, Liu X and Lin Z 2017 Recent advances in interfacial engineering of perovskite solar cells *J. Phys. D: Appl. Phys.* **50** 373002
[6]   Han C, Wang K, Zhu X, Yu H, Sun X, Yang Q and Hu B 2018 Unraveling surface and bulk trap states in lead halide perovskite solar cells using impedance spectroscopy *J. Phys. D: Appl. Phys.* **51** 095501
[7]   Ono L K and Qi Y B 2018 Research progress on organic–inorganic halide perovskite materials and solar cells *J. Phys. D. Appl. Phys.* **51** 093001
[8]   Ono L K and Qi Y B 2016 Surface and Interface Aspects of Organometal Halide Perovskite Materials and Solar Cells *J. Phys. Chem. Lett.* **7** 4764-94
[9]   Kojima A, Teshima K, Shirai Y and Miyasaka T 2009 Organometal Halide Perovskites as Visible-Light Sensitizers for Photovoltaic Cells *J. Am. Chem. Soc.* **131** 6050-1
[10]   Kim H S, Lee C R, Im J H, Lee K B, Moehl T, Marchioro A, Moon S J, Humphry-Baker R, Yum J H, Moser J E, Grätzel M and Park N G 2012 Lead Iodide Perovskite Sensitized All-Solid-State Submicron Thin Film Mesoscopic Solar Cell with Efficiency Exceeding 9% *Sci. Rep.* **2** 591
[11]   Lee M M, Teuscher J, Miyasaka T, Murakami T N and Snaith H J 2012 Efficient Hybrid Solar Cells Based on Meso-Superstructured Organometal Halide Perovskites *Science* **338** 643-7
[12]   Heo J H, Im S H, Noh J H, Mandal T N, Lim C S, Chang J A, Lee Y H, Kim H J, Sarkar A, Nazeeruddin M K, Gratzel M and Seok S I 2013 Efficient Inorganic-Organic Hybrid Heterojunction Solar Cells Containing Perovskite Compound and Polymeric Hole Conductors *Nat. Photonics* **7** 487-92
[13]   National Renewable Energy Laboratory (NREL). Research Cell Efficiency Records. *http://www.nrel.gov/ncpv/images/efficiency_chart.jpg* (Last date accessed: May 14th, 2018)
[14]   Berhe T A, Su W-N, Chen C-H, Pan C-J, Cheng J-H, Chen H-M, Tsai M-C, Chen L-Y, Dubale A A and Hwang B-J 2016 Organometal Halide Perovskite Solar Cells: Degradation and Stability *Energy Environ. Sci.* **9** 323-56

[15]   Hawash Z, Ono L K and Qi Y B 2018 Recent Advances in Spiro-MeOTAD Hole Transport Material and Its Applications in Organic-inorganic Halide Perovskite Solar Cells *Adv. Mater. Interfaces* **5** 1700623

[16]   Cappel U B, Daeneke T and Bach U 2012 Oxygen-Induced Doping of Spiro-MeOTAD in Solid-State Dye-Sensitized Solar Cells and Its Impact on Device Performance *Nano Lett.* **12** 4925-31

[17]   Hawash Z, Ono L K and Qi Y B 2016 Moisture and Oxygen Enhance Conductivity of LiTFSI-Doped Spiro-MeOTAD Hole Transport Layer in Perovskite Solar Cells *Adv. Mater. Interfaces* **3** 1600117

[18]   Zhao X, Kim H-S, Seo J-Y and Park N-G 2017 Effect of Selective Contacts on the Thermal Stability of Perovskite Solar Cells *ACS Appl. Mater. Interfaces* **9** 7148-53

[19]   Sanchez R S and Mas-Marza E 2016 Light-Induced Effects on Spiro-OMeTAD Films and Hybrid Lead Halide Perovskite Solar Cells *Sol. Energy Mater. Sol. Cells* **158** 189-94

[20]   Jena A K, Numata Y, Ikegami M and Miyasaka T 2018 Role of spiro-OMeTAD in performance deterioration of perovskite solar cells at high temperature and reuse of the perovskite films to avoid Pb-waste *J. Mater. Chem. A* **6** 2219-30

[21]   Jena A K, Ikegami M and Miyasaka T 2017 Severe Morphological Deformation of Spiro-OMeTAD in $(CH_3NH_3)PbI_3$ Solar Cells at High Temperature *ACS Energy Lett.* **2** 1760-1

[22]   Domanski K, Correa-Baena J-P, Mine N, Nazeeruddin M K, Abate A, Saliba M, Tress W, Hagfeldt A and Grätzel M 2016 Not All That Glitters Is Gold: Metal-Migration-Induced Degradation in Perovskite Solar Cells *ACS Nano* **10** 6306-14

[23]   Ono L K, Schulz P, Endres J J, Nikiforov G O, Kato Y, Kahn A and Qi Y B 2014 Air-Exposure-Induced Gas-Molecule Incorporation into Spiro-MeOTAD Films *J. Phys. Chem. Lett.* **5** 1374-9

[24]   Hawash Z, Ono L K, Raga S R, Lee M V and Qi Y B 2015 Air-Exposure Induced Dopant Redistribution and Energy Level Shifts in Spin-Coated Spiro-MeOTAD Films *Chem. Mater.* **27** 562-9

[25]   Kato Y, Ono L K, Lee M V, Wang S H, Raga S R and Qi Y B 2015 Silver Iodide Formation in Methyl Ammonium Lead Iodide Perovskite Solar Cells with Silver Top Electrodes *Adv. Mater. Interfaces* **2** 1500195

[26]   Jung M C, Raga S R, Ono L K and Qi Y B 2015 Substantial Improvement of Perovskite Solar Cells Stability by Pinhole-Free Hole Transport Layer with Doping Engineering *Sci. Rep.* **5** 9863

[27]   Ono L K, Raga S R, Remeika M, Winchester A J, Gabe A and Qi Y B 2015 Pinhole-Free Hole Transport Layers Significantly Improve the Stability of $MAPbI_3$-Based Perovskite Solar Cells Under Operating Conditions *J. Mater. Chem. A* **3** 15451-6

[28]   Pham H D, Wu Z, Ono L K, Manzhos S, Feron K, Motta N, Qi Y and Sonar P 2017 Low-Cost Alternative High-Performance Hole-Transport Material for Perovskite Solar Cells and Its Comparative Study with Conventional SPIRO-OMeTAD *Adv. Electron. Mater.* **3** 1700139

[29]   Liu M Z, Johnston M B and Snaith H J 2013 Efficient Planar Heterojunction Perovskite Solar Cells by Vapour Deposition *Nature* **501** 395-8

[30]   Divitini G, Cacovich S, Matteocci F, Cinà L, Di Carlo A and Ducati C 2016 In situ Observation of Heat-Induced Degradation of Perovskite Solar Cells *Nat. Energy* **1** 15012

[31]   Sanehira E M, Tremolet de Villers B J, Schulz P, Reese M O, Ferrere S, Zhu K, Lin L Y, Berry J J and Luther J M 2016 Influence of Electrode Interfaces on the Stability of Perovskite Solar Cells: Reduced Degradation Using MoO_x/Al for Hole Collection *ACS Energy Lett.* 38-45

[32]   Juarez-Perez E J, Hawash Z, Raga S R, Ono L K and Qi Y B 2016 Thermal Degradation of $CH_3NH_3PbI_3$ Perovskite into NH_3 and CH_3I Gases Observed by Coupled Thermogravimetry-Mass Spectrometry Analysis *Energy Environ. Sci.* **9** 3406-10

[33]   Juarez-Perez E J, Leyden M R, Wang S, Ono L K, Hawash Z and Qi Y B 2016 Role of the Dopants on the Morphological and Transport Properties of Spiro-MeOTAD Hole Transport Layer *Chem. Mater.* **28** 5702-9

[34]   Wang S, Sina M, Parikh P, Uekert T, Shahbazian B, Devaraj A and Meng Y S 2016 Role of 4-tert-Butylpyridine as a Hole Transport Layer Morphological Controller in Perovskite Solar Cells *Nano Lett.* **16** 5594-600

[35] Toolan D T W and Howse J R 2013 Development of *in situ* Studies of Spin Coated Polymer Films *J. Mater. Chem. C* **1** 603-16

[36] Henrie J, Kellis S, Schultz S M and Hawkins A 2004 Electronic color charts for dielectric films on silicon *Opt. Express* **12** 1464-9

[37] *Solvent Stabilizer System, Sigma-Aldrich, http://www.sigmaaldrich.com/chemistry/solvents/learning-center/stabilizer-systems.html*

[38] Leyden M R, Ono L K, Raga S R, Kato Y, Wang S H and Qi Y B 2014 High Performance Perovskite Solar Cells by Hybrid Chemical Vapor Deposition *J. Mater. Chem. A* **2** 18742-5

[39] Leyden M R, Lee M V, Raga S R and Qi Y B 2015 Large Formamidinium Lead Trihalide Perovskite Solar Cells Using Chemical Vapor Deposition with High Reproducibility and Tunable Chlorine Concentrations *J. Mater. Chem. A* **3** 16097-103

[40] Leyden M R, Jiang Y and Qi Y B 2016 Chemical Vapor Deposition Grown Formamidinium Perovskite Solar Modules with High Steady State Power and Thermal Stability *J. Mater. Chem. A* **4** 13125-32

[41] Jiang Y, Leyden M R, Qiu L, Wang S, Ono L K, Wu Z, Juarez-Perez E J and Qi Y B 2018 Combination of Hybrid CVD and Cation Exchange for Up-Scaling Cs-Substituted Mixed Cation Perovskite Solar Cells with High Efficiency and Stability *Adv. Func. Mater.* **27** 1703835

[42] Juarez-Perez E J, Ono L K, Maeda M, Jiang Y, Hawash Z and Qi Y 2018 Photo-, Thermal-decomposition in Methylammonium Halide Lead Perovskites and inferred design principles to increase photovoltaic device stability *J. Mater. Chem. A* DOI: 10.1039/C8TA03501F

[43] Reisdorffer F, Haas O, Le Rendu P and Nguyen T P 2012 Co-solvent effects on the morphology of P3HT:PCBM thin films *Synth. Met.* **161** 2544-8

[44] Motaung D E, Malgas G F and Arendse C J 2010 Comparative study: The effects of solvent on the morphology, optical and structural features of regioregular poly(3-hexylthiophene):fullerene thin films *Synth. Met.* **160** 876-82

[45] Birnie D P 2013 A Model for Drying Control Cosolvent Selection for Spin-Coating Uniformity: The Thin Film Limit *Langmuir* **29** 9072-8

[46] Stange T G, Evans D F and Hendrickson W A 1997 Nucleation and Growth of Defects Leading to Dewetting of Thin Polymer Films *Langmuir* **13** 4459-65

[47] Scriven L E 1988 Physics and Applications of Dip Coating and Spin Coating *Mat. Res. Soc. Symp. Proc.* **121** 717-29

[48] Norrman K, Ghanbari-Siahkali A and Larsen N B 2005 6 Studies of spin-coated polymer films *Annu. Rep. Prog. Chem. C* **101** 174-201

[49] Bornside D E, Macosko C W and Scriven L E 1989 Spin coating: One-dimensional model *J. Appl. Phys.* **66** 5185-93

[50] Flack W W, Soong D S, Bell A T and Hess D W 1984 A mathematical model for spin coating of polymer resists *J. Appl. Phys.* **56** 1199-206

[51] Na J Y, Kang B, Sin D H, Cho K and Park Y D 2015 Understanding Solidification of Polythiophene Thin Films during Spin-Coating: Effects of Spin-Coating Time and Processing Additives *Sci. Rep.* **5** 13288

[52] Gaikwad A M, Khan Y, Ostfeld A E, Pandya S, Abraham S and Arias A C 2016 Identifying orthogonal solvents for solution processed organic transistors *Org. Electron.* **30** 18-29

[53] Dualeh A, Moehl T, Tétreault N, Teuscher J, Gao P, Nazeeruddin M K and Grätzel M 2014 Impedance Spectroscopic Analysis of Lead Iodide Perovskite-Sensitized Solid-State Solar Cells *ACS Nano* **8** 362-73

[54] Chen D Y, Tseng W H, Liang S P, Wu C I, Hsu C W, Chi Y, Hung W Y and Chou P T 2012 Application of F4TCNQ doped spiro-MeOTAD in high performance solid state dye sensitized solar cells *Phys. Chem. Chem. Phys.* **14** 11689-94

[55] Olson C, Veldman D, Bakker K and Lenzmann F 2011 Characterization of the Pore Filling of Solid State Dye Sensitized Solar Cells with Photoinduced Absorption Spectroscopy *Int. J. Photoenergy* **2011** 513089

[56] Snaith H J, Humphry-Baker R, Chen P, Cesar I, Zakeeruddin S M and Grätzel M 2008 Charge collection and pore filling in solid-state dye-sensitized solar cells *Nanotechnology* **19** 424003

[57] Qiu L, Ono L K and Qi Y B 2017 Advances and challenges to the commercialization of organic–inorganic halide perovskite solar cell technology *Mater. Today Energy* **7** 169-89

[58]   Bijal B P and Ying D 2018 Multiscale assembly of solution-processed organic electronics: the
        critical roles of confinement, fluid flow, and interfaces *Nanotechnology* **29** 044004
[59]   Chang M, Lim G, Park B and Reichmanis E 2017 Control of Molecular Ordering, Alignment,
        and Charge Transport in Solution-Processed Conjugated Polymer Thin Films *Polymers* **9** 212
[60]   Diao Y, Shaw L, Bao Z and Mannsfeld S C B 2014 Morphology Control Strategies for Solution-
        Processed Organic Semiconductor Thin Films *Energy Environ. Sci.* **7** 2145-59
[61]   Semaltianos N G 2007 Spin-coated PMMA films *Microelectron. J.* **38** 754-61

TOC Figure: